Journal Name

ARTICLE TYPE

Cite this: DOI: 00.0000/xxxxxxxxxx

Received Date
Accepted Date

DOI: 00.0000/xxxxxxxxxx

Theoretical Modeling of Structural Superlubricity in Rotated Bilayer Graphene, Hexagonal Boron Nitride, Molybdenum Disulfide, and Blue Phosphorene

Tilas Kabengele[a] and Erin R. Johnson[a,b,*]

The superior lubrication capabilities of two-dimensional crystalline materials such as graphene, hexagonal boron nitride (h-BN), and molybdenum disulfide (MoS_2) have been well known for many years. It is generally accepted that structural superlubricity in these materials is due to misalignment of the surfaces in contact, known as incommensurability. In this work, we present a detailed study of structural superlubricity in bilayer graphene, h-BN, MoS_2, and the novel material blue phosphorene (b-P) using dispersion-corrected density-functional theory with periodic boundary conditions. Potential energy surfaces for interlayer sliding were computed for the standard (1×1) cell and the three rotated, Moiré unit cells for each material. The energy barriers to form the rotated structures remain higher than the minimum-energy sliding barriers for the (1×1) cells. However, if the rotational barriers can be overcome, nearly barrierless interlayer sliding is observed in the rotated cells for all four materials. This is the first density-functional investigation of friction using rotated, Moiré cells, and the first prediction of structural superlubricty for b-P.

1 Introduction

Overcoming friction is a universal problem in any mechanical system due to the resulting wear to the moving parts, unwanted heat, and energy losses. Of the annual global energy consumption (about 400 exajoules), approximately 20% (103 exajoules) is lost to friction.[1–4] Consequently, implementing better friction-reduction techniques would lead to cost savings, while also reducing CO_2 emissions worldwide. These prospects to better the economy and the environment have fueled both theoretical and experimental research in modern tribology.

The frictional properties of solid lubricants, such as graphite and MoS_2, have been widely studied for many years. Fundamentally, the force of friction originates from molecular interactions between constituent atoms of solids due to atomistic locking.[5] The phenomenon of structural superlubricity,[6–8] where friction completely vanishes for incommensurate interactions between two clean, atomically flat surfaces, was predicted[5,9] and subsequently verified experimentally in graphite[10–12] and other layered materials.[13–19]

Experimental surface-force techniques, such as atomic force microscopy, are typically used to investigate frictional properties of layered two-dimensional (2D) materials and surfaces. In an experimental investigation of the frictional properties of graphite, Dienwiebel *et al.*[10] examined the energy dissipation between the tip of a frictional force microscope (FFM) sliding over a graphite surface under a dry nitrogen atmosphere. They measured the atomic-scale friction as a function of the rotational angle between the tip and the top layer of the graphite surface, and found ultra-low friction regimes between rotated graphite layers. Similar studies have been conducted on a wide range of 2D materials, including MoS_2,[16] and heterostructures of graphene with h-BN.[17,18] These studies have demonstrated that structural superlubricity results from the incommensurability of the surfaces in contact.

However, keeping structures in an incommensurate state is a tremendous practical challenge as structural deformations occur at the interface of the overlayer and substrate during sliding. When the contact starts undergoing deformation, incommensurate states can be terminated, leading to the reorientation of the structure back into a commensurate high-friction configuration.[20] Such deformations are more significant in larger systems, and increase with normal load, temperature, and pressure.[21–26] This is a major impediment to achieving superlubricity at scales suitable for any practical applications.[8,27]

Further theoretical and experimental work is needed to gain a better understanding of the atomic-scale processes at the sliding interface. Notably, Claerbout *et al.*[28] recently suggested a novel mechanism for achieving low friction in commensurate MoS_2, and concluded that incommensurability may not be a require-

---

[a] *Department of Physics and Atmospheric Science, Dalhousie University, 6310 Coburg Road, Halifax, Nova Scotia, Canada B3H 4R2.*

[b] *Department of Chemistry, Dalhousie University, 6274 Coburg Road, Halifax, Nova Scotia, Canada B3H 4R2. E-mail: erin.johnson@dal.ca*

ment for superlubricity. In their work, ultra-low friction regimes were achieved by varying the direction of the driving force during a classical molecular-dynamics (MD) simulation involving commensurate MoS_2 layers.

MD is a computational approach that is widely used to study the frictional properties of surfaces and interfaces.[29–34] Classical MD simulations describe the interaction energy and dynamics of atoms using Newtonian mechanics. It is possible to set a variety of parameters, e.g. normal load, velocity, temperature, contact area, compliance (relationship between force and stiffness in AFM experiments), and other properties. Different materials are specified by assigning empirical potentials fit to the system being investigated. Numerous potentials optimized for various purposes are available, including the Lennard-Jones (LJ) potential,[35] the Embedded Atom Method (EAM),[36] the reactive empirical bond-order (REBO) potential,[37] the adaptive intermolecular REBO potential,[38] and ReaxFF,[39] among others.

Classical MD simulations provide a good approximation of the dynamic and mechanical properties of a system. However, choosing an accurate empirical potential is critical to predicting realistic behaviour. Due to the numerous empirical potentials and parameters that exist, researchers need to be able to carefully evaluate the efficacy and accuracy of these models. Since MD simulations rely heavily on empirical parameters and do not fully capture the quantum mechanical features of the system (e.g. chemical bonding, Pauli repulsion, and London dispersion forces), they are less accurate than electronic-structure methods, such as density-functional theory (DFT).

From a first-principles approach, the frictional behavior of 2D materials can be studied by modelling the potential energy surface (PES) of the given system.[40–45] For interlayer sliding of a 2D material, the PES is defined by translation of the overlayer atop the substrate. At each static point on the PES, the atomic positions are optimized to minimize the electronic energy of the system. PES computed from DFT can be used to validate empirical potentials employed in classical MD, and can also be used as input for simple nanoscale models of friction, such as the Prandtl–Tomlinson (PT) and Frenkel–Kontorova (FK) models.[46–49] However, DFT calculations are computationally expensive and their utility is confined to periodic systems when planewave basis sets are employed, prohibiting application to incommensurate structures. This limitation is circumvented by analyzing the Moiré patterns formed when the overlayer is rotated with respect to the substrate.[50–52] It is then possible to define computationally tractable, rotated unit cells with properties expected to resemble those of incommensurate interfaces and, hence, show superlubricity.

In this work, we use dispersion-corrected DFT to investigate structural superlubricity in rotated bilayers of graphene, h-BN, MoS_2, and blue phosphorene (b-P). We model the sliding PES for Moiré cells of these materials with 0°, 13.17°, 21.79°, and 32.20° relative rotation angles. Additionally, we compute the exfoliation energy and rotation barriers of each material. We show that commensurate sliding of 2D materials along very specific trajectories results in small barriers, suggesting that incommensurability is not required for low friction. However, drastically lower sliding barriers are found for the rotated cells. These results confirm superlubricity for rotated graphene, MoS_2, and h-BN, and we report the first prediction of superlubricity for the novel material b-P.

Table 1 Commensurate structures of bilayer graphene, h-BN, MoS_2, and b-P with 0° rotation of the top layer.[56]

Material	View 1	View 2	View 3
Graphene	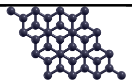	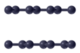	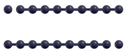
h-BN	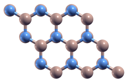	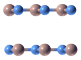	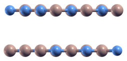
MoS_2	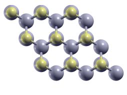	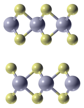	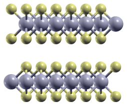
b-P	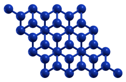	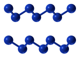	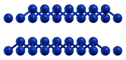

Table 2 The (m,n) parameters and the relative rotation angles, φ, of the overlayer to the substrate for the Moiré unit cells. The numbers of atoms in the graphene, h-BN, and b-P unit cells are also shown; the MoS_2 unit cells contain 1.5 times more atoms.

(m,n)	φ (degrees)	Atoms
(1×1)	0.00	4
$(2,1)$	21.79	28
$(3,1)$	32.20	52
$(3,2)$	13.17	76

2 Computational Methods

2.1 Unrotated Structures, $\varphi = 0^\circ$

Crystal structures for graphite, h-BN, and MoS_2 were obtained from the crystallographic open database (COD)[53]. The structure for b-P was constructed based on known parameters in the literature.[54,55] Graphene, h-BN, MoS_2, and b-P have hexagonal unit cells with x,y-lattice parameters, $a_\circ$, of 2.47, 2.51, 3.15, and 3.33 Å, respectively. Bilayer structures of the materials were generated by inserting a large vacuum region, such that all unit cells spanned 80 Bohr (42.33 Å) in the z direction. The relative rotation angle of the overlayer to the substrate, φ, is implicitly 0° in this case. Table 1 shows the unrotated structures of these materials.

2.2 Rotated Structures, $\varphi \neq 0^\circ$

Rotating the overlayer with respect to the substrate creates Moiré patterns.[50] Appropriate choices of rotation angle allow definition of sufficiently small unit cells to allow us to perform planewave DFT calculations, which require periodic boundary conditions.

Obtaining Moiré unit cells for hexagonal lattices through the rotation of one layer with respect to the other has been discussed at length elsewhere.[51,52] We let $\mathbf{a}_\circ$ and $\mathbf{b}_\circ$ be the lattice vectors of the (1×1) cell of a given material. The full range of the possible unit cells is given by two parameters, (m,n), used to define the

Table 3 Rotated structures of graphene, h-BN, MoS_2, and b-P.[56]

(m,n)	$(2,1)$	$(3,1)$	$(3,2)$
Graphene	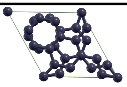	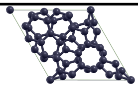	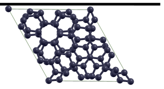
h-BN	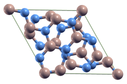	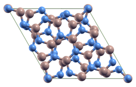	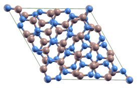
MoS_2	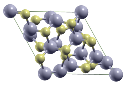	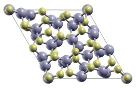	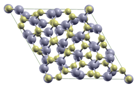
b-P	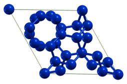	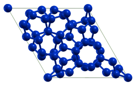	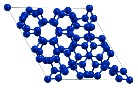

lattice vectors of the resulting Moiré unit cell:

$$\mathbf{a}_m = m\mathbf{a}_\circ + n\mathbf{b}_\circ \tag{1}$$

and

$$\mathbf{b}_m = -n\mathbf{a}_\circ + (m+n)\mathbf{b}_\circ, \tag{2}$$

where $m,n \in N$, and $m > n$. The rotation angle for the hexagonal Moiré cell is then evaluated as

$$\cos(\varphi) = \frac{m^2 + 4mn + n^2}{2(n^2 + mn + m^2)}. \tag{3}$$

We implemented the scheme described above in a `python` program to obtain rotated structures with (m,n) parameters of $(2,1)$, $(3,1)$, and $(3,2)$ for each material. These correspond to relative rotation angles of 21.79°, 32.20°, and 13.17°, respectively. Tables 2 and 3 show the number of atoms in the respective Moiré unit cells, and the top views of these structures, respectively.

2.3 Density-Functional Theory

All DFT calculations in this work were carried out with the projector augmented-wave approach[57,58] and the B86bPBE[59,60] exchange-correlation functional using Quantum ESPRESSO.[61] The eXchange-hole Dipole Moment (XDM) model,[62–64] previously shown to be highly accurate for properties of layered materials,[65] was used to account for dispersion interactions. The total electronic energy can then be written as

$$E = E_{\text{base}} + E_{\text{disp}}, \tag{4}$$

where E_{base} is the contribution from the base B86bPBE density functional, which includes electrostatics and non-bonded repulsion, while E_{disp} is the XDM dispersion energy. The XDM damping parameters were taken as their canonical values for use with the B86bPBE functional ($a_1 = 0.6512$, $a_2 = 1.4633$ Å).

The planewave cutoff energies were set to 80 Ry for the wave functions and 800 Ry for the electron density. All calculations used uniform k-point sampling, with $8 \times 8 \times 1$, $6 \times 6 \times 1$, $4 \times 4 \times 1$, and $2 \times 2 \times 1$ meshes selected for the 4-atom, 28-atom, 52-atom, and 76-atom unit cells, respectively. For MoS_2, k-point meshes of $8 \times 8 \times 1$, $4 \times 4 \times 1$, $2 \times 2 \times 1$, and $1 \times 1 \times 1$ were used for the 6-atom, 42-atom, 78-atom, and 114-atom unit cells, respectively. For geometry relaxations, the convergence thresholds were set to 10^{-5} Ry for the energy and 10^{-4} Ry/Bohr for the forces.

For both the (1×1) and rotated cells, all atomic positions were relaxed with the cell parameters held fixed. 2D sliding of each material was then modeled by gradually translating the atoms comprising the overlayer along the long diagonal of the unit cell in a series of 50 increments. During sliding, the x,y atomic positions were held fixed, with the z atomic positions allowed to relax at each point to properly determine the interaction energy between the layers in the z (normal) direction. The minimum energy points on the resulting potential energy surfaces were then identified and used to evaluate the rotation barriers and exfoliation energies.

The rotation barriers were computed as

$$\Delta E_{\text{rot}} = E_{\text{min,rotated}} - E_{\text{min,unrotated}}, \tag{5}$$

where $E_{\text{min,rotated}}$ and $E_{\text{min,unrotated}}$ are the minimum energies obtained for the rotated and unrotated geometries. The exfoliation energies (i.e. the energy required to separate the layers) for the unrotated cells were evaluated using

$$\Delta E_{\text{ex}} = E_{\text{min,unrotated}} - 2E_{\text{monolayer}}, \tag{6}$$

where $E_{\text{monolayer}}$ is the energy of a single layer. The rotation and exfoliation energies are typically expressed either per atom or per unit area. For a hexagonal cell, the area is $A = (\sqrt{3}/2)a_\circ^2$.

3 Results and Discussions

3.1 Exfoliation Energies

Exfoliation energies were computed for the (1×1) unit cell of each bilayer according to Eqn. 6. Table 4 shows the exfoliation energies, along with a decomposition into the base density-functional and XDM dispersion terms. The base functional contributions are all positive, as expected since dispersion is responsible for binding of these layered materials. In the absence of the XDM dispersion correction, there would be no binding between the layers, since the base B86bPBE functional is dispersionless. The dispersion energy is larger in magnitude than the total exfoliation energy, as dispersion must also compensate for the non-bonded repulsion between the layers arising from the base functional.

The overall trend in the magnitude of the dispersion energies (per atom) is graphene<h-BN<b-P<MoS_2, while for the total exfoliation energies, this trend is changed to graphene<b-P<h-BN<MoS_2. The base functional repulsion is lower for h-BN than for the other three materials since it adopts a stacked configuration to maximize favourable electrostatic interactions, rather than a staggered configuration to maximize dispersion (see Table 1).

3.2 Sliding PES Without Rotation, $\varphi = 0°$

Figure 1 shows the PES for interlayer sliding of the unrotated (1×1) unit cells. Similar results have been reported previously for graphene, h-BN, and MoS_2.[42] For each material, two minima are obtained at fractional sliding coordinates of 0 and 2/3, while two maxima, corresponding to high- and low-friction peaks, are seen at fractional coordinates of 1/3 and 5/6, respectively. The

Fig. 1 Potential energy surfaces for interlayer sliding of the unrotated unit cells (black lines) of (a) graphene, (b) h-BN, (c) MoS_2, and (d) b-P. The horizontal lines represent the rotation barriers for each cell, while the purple line (Avg) is the average of the black curve over all the full PES. Note the larger y-axis scale for MoS_2 and b-P compared to graphene and h-BN.

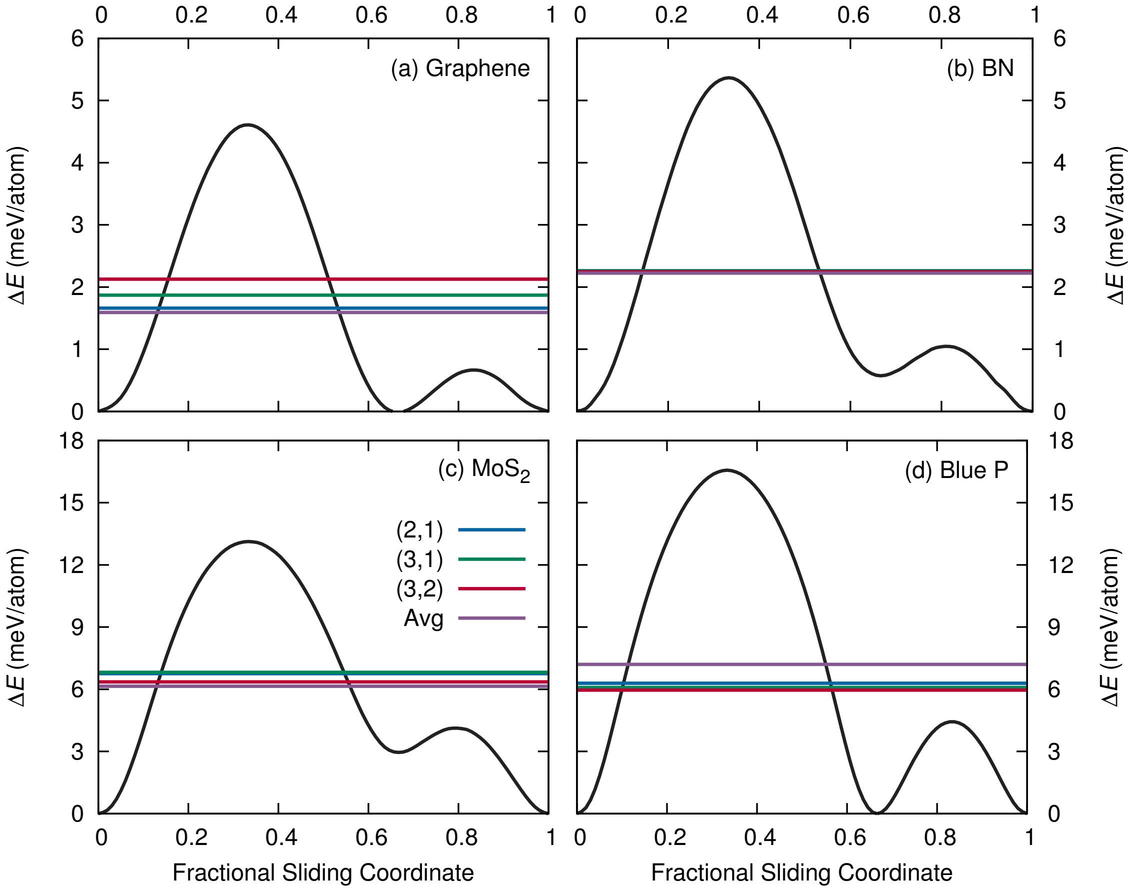

Table 4 Total exfoliation energies of the bilayer materials, in meV/atom, as well as the separate base-functional and dispersion contributions. Values in meV/Å^2 are given in parentheses.

Material	Total	Base	Dispersion
Graphene	-24.4 (-18.5)	8.5 (6.4)	-32.9 (-24.9)
h-BN	-29.4 (-21.6)	5.7 (4.2)	-35.1 (-25.7)
MoS_2	-32.5 (-22.7)	11.1 (7.8)	-43.6 (-30.4)
b-P	-25.6 (-10.7)	14.5 (6.0)	-40.1 (-16.7)

geometries of these stationary points are shown in Table 5.

For graphene, the two minima are degenerate (i.e. equal in energy) and have the atomic layers staggered to maximize dispersion interactions while minimizing non-bonded repulsion. The global maximum has the layers stacked so that the atoms are perfectly aligned in the z direction. Conversely, for h-BN, the global minimum has the layers aligned with B atoms located directly above or below the N atoms of the other layer to maximize favourable electrostatic interactions. The higher-energy local minimum for h-BN has the B atoms vertically aligned, but the N atoms staggered, while the global maximum has the N atoms vertically aligned and the B atoms staggered. The global minimum for MoS_2 also has stacked layers, with the S atoms from one layer vertically aligned above or below the Mo atoms of the other layer. In the local minimum configuration, the Mo atoms are aligned and the S atoms staggered, to minimize repulsion between the more electronegative S atoms, whereas the S atoms are aligned and the Mo atoms staggered in the global maximum configuration. Finally, the stationary points for b-P resemble those of graphene, with staggered layers for the two degenerate minima and aligned layers for the global maximum.

The sliding barriers, defined as the energy differences between the maxima and minima on the PES, should be directly related to the frictional behaviour of the materials. From Figure 1, MoS_2 and b-P have sliding barriers approximately 3 times larger than those seen for the graphene and h-BN PES. Unlike graphene and h-BN, the atomically thin layers in MoS_2 and b-P are corrugated, leading to a greater contact area and, hence, greater friction. The overall trend for the sliding barriers is graphene<h-BN<MoS_2 <b-P.

The two saddle points on the PES in Figure 1 show that the top layer feels different energy barriers as it slides over different regions of the substrate within the unrotated, commensurate unit cell. This means that, for unrotated structures, sliding in different directions can yield remarkably different frictional behaviours. Using classical MD, Claerbout *et al.*[28] recently showed that applying a driving force in different sliding directions can drastically alter the friction in commensurate MoS_2. In their work, a

Table 5 Geometries of stationary points on the interlayer sliding PES for unrotated, (1×1) unit cells.[56]

Material	Global Minimum	Global Maximum	Local Minimum	Local Maximum
Graphene	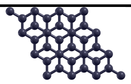	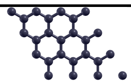	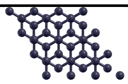	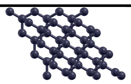
h-BN	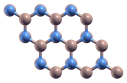	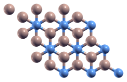	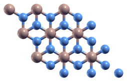	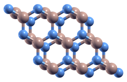
MoS_2	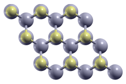	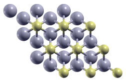	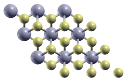	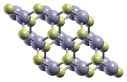
b-P	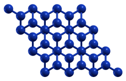	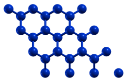	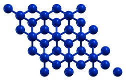	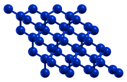

Fig. 2 Representative 2D potential energy surface for commensurate sliding of a layered material using the unrotated (1×1) cell. The anistropy of the PES leads to different coefficients of friction for different sliding directions. The lowest friction is obtained for the zig-zag paths corresponding to 30° and 90° sliding trajectories, while the highest friction is obtained for 0° and 60° trajectories.

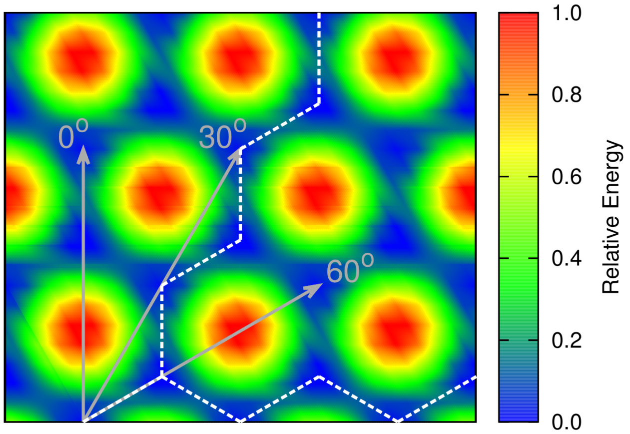

low-friction regime was found when the overlayer slid in a zig-zag path that avoided the higher energy barrier on the potential energy surface, as shown in Figure 2. Their findings are consistent with the results in this work. The PES in Figure 1 demonstrate that similar energetically favorable sliding paths exist for unrotated, commensurate graphene, h-BN, MoS_2, and b-P.

3.3 Rotation Energies

The rotation barrier, computed using equation 5, is the minimum energy required to obtain a Moiré structure, by means of rotating the overlayer with respect to its substrate. These barriers allow us to assess the stability of the Moiré cells, relative to the (1×1) cells. Table 6 shows the total rotation energies, as well as the base-functional and dispersion contributions, for each material and rotation angle considered. Similar to the exfoliation energy, the rotation barriers are dominated by dispersion interactions. For graphene and h-BN, the base-functional contributions to the rotation energies are negligible due to the planarity of the 2D atomic layers. The magnitudes of the total and component rotation energies for MoS_2 and b-P are much larger than for graphene and h-BN due to the corrugated nature of the 2D layers in the former two materials.

Table 6 Total rotation energies, in meV/atom, as well as the base-functional and dispersion contributions.

Material	(m,n)	Total	Base	Dispersion
Graphene	$(2,1)$	1.66	0.06	1.60
	$(3,1)$	1.87	0.37	1.50
	$(3,2)$	2.13	0.35	1.78
h-BN	$(2,1)$	2.26	0.11	2.16
	$(3,1)$	2.26	0.11	2.16
	$(3,2)$	2.25	0.12	2.12
MoS_2	$(2,1)$	6.75	-2.12	8.87
	$(3,1)$	6.82	-2.04	8.86
	$(3,2)$	6.36	-2.20	8.56
b-P	$(2,1)$	6.29	-3.80	10.09
	$(3,1)$	6.09	-4.68	10.77
	$(3,2)$	5.96	-3.88	9.85

In the minimum-energy configurations of the (1×1) cells, the MoS_2 and b-P layers are interlocking, allowing close interlayer distances that maximize dispersion attraction. Conversely, in the rotated cells, the layers cannot interlock due to their misalignment. This results in larger interlayer distances (by ca. 0.25 Å in MoS_2 and 0.40 Å in b-P, see Table 7), which decreases the magnitudes of both dispersion attraction and non-bonded repulsion. Hence, there is a negative contribution to the rotation energy from the base functional due to reduced repulsion in the rotated cell. This is offset by the much greater reduction in dispersion binding, resulting in higher total rotation barriers.

The rotation barriers for each Moiré cell are also shown in Figure 1 and are consistently higher than the minimum sliding barriers for each material. We additionally find that the rotation barriers are comparable to the average value of the sliding PES for each of the four materials. This can be rationalized through understanding of the interlayer contacts. As noted above, the unrotated PES show two distinct maxima, which correspond to high and low frictional contacts. However, when the overlayer is rotated, these distinct contacts are disrupted, resulting in a structure with an even mixture of favourable and unfavourable interlayer contacts. The interlayer interactions of the rotated structure will therefore be a distribution over all the contact points, and the

Table 7 Interlayer separation between the top and bottom layers. The minimum ($d_{\min}$), maximum ($d_{\max}$), and average (d_{avg}) z-distances over all the data points in each PES scan are shown. (1×1) denotes the unrotated unit cells.

Material	(m,n)	$d_{\min}$	$d_{\max}$	Δd	d_{avg}
Graphene	(1×1)	3.38	3.57	**0.19**	3.45
	$(2,1)$	3.43	3.43	0.00	3.43
	$(3,1)$	3.43	3.43	0.00	3.43
	$(3,2)$	3.43	3.43	0.00	3.43
h-BN	(1×1)	3.29	3.51	**0.22**	3.37
	$(2,1)$	3.37	3.37	0.00	3.37
	$(3,1)$	3.37	3.37	0.00	3.37
	$(3,2)$	3.34	3.35	0.01	3.34
MoS_2	(1×1)	2.99	3.60	**0.61**	3.24
	$(2,1)$	3.27	3.27	0.00	3.27
	$(3,1)$	3.27	3.27	0.00	3.27
	$(3,2)$	3.24	3.27	0.03	3.25
b-P	(1×1)	3.16	4.08	**0.92**	3.55
	$(2,1)$	3.54	3.60	0.06	3.59
	$(3,1)$	3.59	3.62	0.04	3.61
	$(3,2)$	3.43	3.55	0.12	3.51

relative energy of the rotated cell will be approximately equal to the average of all the points on the unrotated PES.

3.4 Interlayer Separation

The idea that the rotated cells involve averaged interatomic contacts is reinforced further by analysis of the interlayer distances during sliding. As the overlayer slides atop the substrate, the vertical interlayer distance, d, changes due to the varying strength of the potential at different relative sliding positions. Table 7 shows the minimum, maximum, and average interlayer distances obtained along the sliding PES for each material and rotation angle. We find that the average interlayer distances for the unrotated (1×1) cells nearly match those of the rotated cells in all cases.

Table 7 also shows the difference between the maximum and the minimum interlayer distances, $\Delta d = d_{\max} - d_{\min}$, for each PES. There is a clear correlation between the Δd values and the maximum sliding barriers. For the (1×1) cells, b-P and MoS_2 show Δd values that are 3-4 times greater than those observed for graphene and h-BN, which is comparable to the observed differences in sliding barriers. Due to their corrugated nature, MoS_2 and b-P have the largest sliding barriers, interlayer-distance differences, and dispersion contributions to the rotation energies (Table 6). Further, the (1×1) unit cells consistently show higher interlayer-distance differences than their rotated counterparts and, as we will see in Sec. 3.5, much higher sliding barriers as well.

3.5 Sliding PES With Rotation, $\varphi \neq 0^\circ$

Figure 3 shows the interlayer-sliding PES for the rotated unit cells of graphene, h-BN, MoS_2, and b-P. While exhibiting Moiré patterns, these structures have clearly defined unit cells, and satisfy the periodic boundary conditions required in planewave DFT codes. We created each unit cell using the (m,n) scheme[51,52], where each combination of integers m and n corresponds to a specific relative rotation angle of the overlayer (see Table 2).

The PES for the $(2,1)$, $(3,1)$, and $(3,2)$ Moiré unit cells for each material display much lower sliding barriers than those obtained for the unrotated PES curves. A superlubric regime was achieved in the rotated cells for each material. For MoS_2 and b-P, which possess corrugated layers, the relative energies across the PES for the rotated cells are are 3-10 times lower than the minimum barriers for the (1×1) cells. Graphene and h-BN, which possess completely planar layers, slid with effectively zero barriers for all the rotated cells and should exhibit ultra-low friction.

We have observed a strong connection between the changes in the interlayer distance reported in Table 7, and the sliding PES peaks. For the rotated cells, virtually no changes in interlayer distance over the sliding PES occurred for graphene and h-BN. For MoS_2, a non-zero distance difference was obtained only for (3,2), which gives the highest sliding barrier. Larger changes in interlayer distance are seen for rotated b-P, but they remain much smaller than for the (1×1) cell. In particular, the $(3,2)$ geometry for b-P showed an interlayer-distance difference greater than 0.1 Å, leading to a sliding potential with relatively high barriers, as shown in Figure 3.

Overall, the materials with the smallest changes in the interlayer distance during sliding (graphene and h-BN) result in the smoothest sliding potentials. This means that the lowest friction will be observed in graphene and h-BN, followed by MoS_2 and b-P. The variation in the frictional properties in the flat versus the corrugated materials can be understood in terms of averaged contacts and surface area. The disruption of high-energy contact points in the rotated geometries leads to removal of the two distinct maxima observed on the unrotated PES curves. As the rotated geometries involve a distribution of favourable and unfavourable contacts along the entire sliding coordinate, the PES peaks are flattened, thereby permitting structural superlubricity in the rotated structures.

4 Conclusions and Outlook

In this work, we investigated friction in both (1×1) and rotated unit cells of graphene, h-BN, MoS_2, and blue-P through density-functional modeling of the potential energy surfaces for interlayer sliding. Higher interlayer sliding barriers are predicted for MoS_2 and blue-P, compared to graphene and h-BN, which is likely due to the corrugation of the layers and the larger contact areas for these two materials. The average of the interlayer distances across the unrotated PES is consistently found to be a good approximation to the interlayer distance in the rotated cells. Similarly, the average of the unrotated sliding potential is found to be good approximation to the rotation energy, since the rotated cells involve both favorable and unfavorable contacts. This distribution of contacts results in a smoothing of the PES, leading to ultra-low friction for the rotated cells.

The PES for the unrotated structures indicate that the zig-zag sliding path (see Figure 2) predicted for unrotated MoS_2 by Claerbout *et al.*[28] should be observed for all 4 materials. However, provided the rotational barriers can be overcome, much lower friction regimes are achieved in the rotated structures. Our findings confirm structural superlubricity in rotated graphene, h-BN, and

Fig. 3 Potential energy surfaces for interlayer sliding of Moiré unit cells of (a) graphene, (b) h-BN, (c) MoS_2, and (d) b-P. Note the larger y-axis scale for MoS_2 and b-P compared to graphene and h-BN.

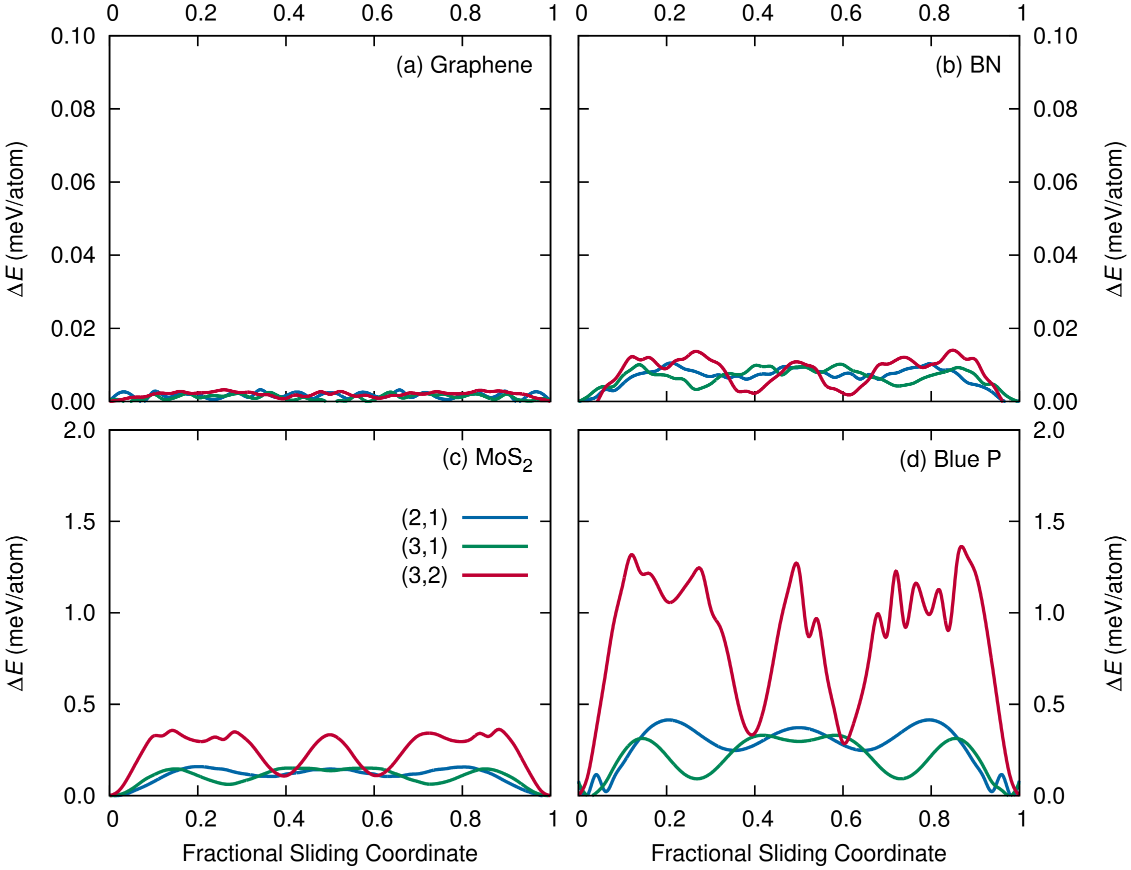

MoS_2, and provide the first prediction of this phenomenon in the novel material b-P for two of the three rotation angles considered.

For many years, incommensurability has been the center of attention in achieving superlubricity in 2D materials. Superlubricity is intrinsically more prominent in heterostructures[18] as it is harder to maintain incommensurability in homogeneous configurations because the lattices are more prone to collapse back into their default commensurate orientations. Since achieving incommensurability in experimental settings is a challenge, perhaps targeting specific rotation angles[66,67] may provide new strategies for achieving superlubricity, and bring us closer to the design of industrially applicable solid superlubricants.

5 Acknowledgements

The authors gratefully acknowledge the Natural Sciences and Engineering Research Council of Canada (NSERC) for financial support and Compute Canada for providing computing resources.

6 Conflicts of interest

The authors declare no conflicts of interest.

Notes and references

1 I. Tzanakis, M. Hadfield, B. Thomas, S. M. Noya, I. Henshaw and S. Austen, *Renew. Sustain. Energy Rev.*, 2012, **16**, 4126 – 4140.
2 K. Holmberg, P. Andersson and A. Erdemir, *Tribol. Int*, 2012, **47**, 221 – 234.
3 K. Holmberg and A. Erdemir, *Frict.*, 2017, **5**, 263–284.
4 K. Holmberg and A. Erdemir, *Tribol. Int*, 2019, **135**, 389 – 396.
5 M. Hirano and K. Shinjo, *Phys. Rev. B*, 1990, **41**, 11837–11851.
6 M. Hirano, *Wear*, 2003, **254**, 932–940.
7 M. H. Müser, *Europhys. Lett.*, 2004, **66**, 97–103.
8 M. Z. Baykara, M. R. Vazirisereshk and A. Martini, *Appl. Phys. Rev.*, 2018, **5**, 041102.
9 K. Shinjo and M. Hirano, *Surf. Sci.*, 1993, **283**, 473–478.
10 M. Dienwiebel *et al.*, *Phys. Rev. Lett.*, 2004, **92**, 11837–11851.
11 M. Dienwiebel, N. Pradeep, G. S.Verhoeven, H. W. Zandbergen and J. W. M. Frenken, *Surf. Sci.*, 2005, **576**, 197–211.
12 Q. Zheng, B. Jiang, S. Liu, Y. Weng, L. Lu, Q. Xue, J. Zhu, Q. Jiang, S. Wang and L. Peng, *Phys. Rev. Lett.*, 2008, **100**, 067205.
13 R. Zhang, Z. Ning, Y. Zhang, Q. Zheng, Q. Chen, H. Xie, Q. Zhang, W. Qian and F. Wei, *Nat. Nanotech.*, 2013, **8**, 912–916.
14 S. Kawai, A. Benassi, E. Gnecco, H. Söde, R. Pawlak, X. Feng, K. Müllen, D. Passerone, C. A. Pignedoli, P. Ruffieux, R. Fasel and E. Meyer, *Science*, 2016, **351**, 957–961.

15 L. Wang, X. Zhou, T. Ma, D. Liu, L. Gao, X. Li, J. Zhang, Y. Hu, H. Wang, Y. Dai and *et al.*, *Nanoscale*, 2017, **9**, 10846–10853.

16 H. Li, J. Wang, S. Gao, Q. Chen, L. Peng, K. Liu and X. Wei, *Adv. Mater.*, 2017, **29**, 1701474.

17 D. Mandelli, I. Leven, O. Hod and M. Urbakh, *Sci. Rep.*, 2017, **7**, 10851.

18 Y. Song, D. Mandelli, O. Hod, M. Urbakh, M. Ma and Q. Zheng, *Nat. Mater.*, 2018, **17**, 894–899.

19 B. Jiang, Z. Zhao, Z. Gong, D. Wang, G. Yu and J. Zhang, *Appl. Surf. Sci.*, 2020, **520**, 146303.

20 A. E. Filippov, M. Dienwiebel, J. W. M. Frenken, J. Klafter and M. Urbakh, *Phys. Rev. Lett.*, 2008, **100**, 046102.

21 A. S. de Wijn, C. Fusco and A. Fasolino, *Phys. Rev. E*, 2010, **81**, 046105.

22 M. M. van Wijk, M. Dienwiebel, J. W. M. Frenken and A. Fasolino, *Phys. Rev. B*, 2013, **88**, 235423.

23 X. Feng, S. Kwon, J. Y. Park and M. Salmeron, *ACS Nano*, 2013, **7**, 1718–1724.

24 M. Ma, A. Benassi, A. Vanossi and M. Urbakh, *Phys. Rev. Lett.*, 2015, **114**, 055501.

25 A. Benassi, M. Ma, M. Urbakh and A. Vanossi, *Scientific reports*, 2015, **5**, 16134.

26 T. A. Sharp, L. Pastewka and M. O. Robbins, *Phys. Rev. B*, 2016, **93**, 121402.

27 A. Vanossi, C. Bechinger and M. Urbakh, *Nat. Commun.*, 2020, **11**, 4657.

28 V. E. P. Claerbout, T. Polcar and P. Nicolini, *Comput. Mater. Sci.*, 2019, **163**, 17 – 23.

29 K. Wang, C. Qu, J. Wang, W. Ouyang, M. Ma and Q. Zheng, *ACS Applied Materials & Interfaces*, 2019, **11**, 36169–36176.

30 G. Ru, W. Qi, K. Tang, Y. Wei and T. Xue, *Tribology International*, 2020, **151**, 106483.

31 J. A. Harrison, C. T. White, R. J. Colton and D. W. Brenner, *Phys. Rev. B*, 1992, **46**, 9700–9708.

32 S. Jun, E. Hiroshi, Y. Masashi and O. Etsuji, *Nanotechnology*, 1998, **9**, 118–123.

33 Q. Li, Y. Dong, D. Perez, A. Martini and R. W. Carpick, *Phys. Rev. Lett.*, 2011, **106**, 126101.

34 Y. Dong, Q. Li and A. Martini, *J. Vac. Sci. Technol. A*, 2013, **31**, 030801.

35 J. E. Lennerd-Jones, *Proc. Phys. Sci.*, 1931, **43**, 461–482.

36 S. D. Murray and M. I. Baskes, *Phys. Rev. B*, 1984, **29**, 6443–6453.

37 D. W. Brenner, *Phys. Rev. B*, 1990, **42**, 9458–9471.

38 S. J. Stuart, A. B. Tutein and J. A. Harrison, *J. Chem. Phys.*, 2000, **112**, 6472–6486.

39 A. T. van Duin, S. Dasgupta, F. Lorant and W. A. Goddard, *J. Phys. Chem. A*, 2001, **105**, 9396–9409.

40 M. Wolloch, G. Feldbauer, P. Mohn, J. Redinger and A. Vernes, *Phys. Rev. B*, 2014, **90**, 195418.

41 J. C. Spear, B. W. Ewers and J. D. Batteas, *Nano Today*, 2015, **10**, 301–314.

42 Z. Ye, A. Otero de la Roza, E. R. Johnson and A. Martini, *Nanotech.*, 2015, **26**, 165701.

43 M. S. Christian and E. R. Johnson, *J. Phys. Chem. C*, 2018, **122**, 8910–8918.

44 H. Sakuma, K. Kawai, I. Katayama and S. Suehara, *Science advances*, 2018, **4**, eaav2268.

45 M. R. Vazirisereshk, H. Ye, Z. Ye, A. Otero-de-la Roza, M. Q. Zhao, Z. Gao, A. C. Johnson, E. R. Johnson, R. W. Carpick and A. Martini, *Nano Lett.*, 2019, **19**, 5496–5505.

46 L. Prandtl, *ZAMM - J. Appl. Math. and Mech.*, 1928, **8**, 85–106.

47 V. L. Popov and J. A. T. Gray, *ZAMM - J. Appl. Math. and Mech.*, 2012, **92**, 683–708.

48 S. Aubry, *Physica D*, 1983, **7**, 240 – 258.

49 S. Aubry and P. Y. Le Daeron, *Physica D*, 1983, **8**, 381 – 422.

50 K. Hermann, *J. Condens. Mat. Phys.*, 2012, **24**, 314210.

51 J. M. Campanera, G. Savini, I. Suarez-Martinez and M. I. Heggie, *Phys. Rev. B*, 2007, **75**, 235449.

52 G. Trambly de Laissardire, D. Mayou and L. Magaud, *Nano Lett.*, 2010, **10**, 804–808.

53 S. Gražulis, D. Chateigner, R. T. Downs, A. F. T. Yokochi, M. Quirós, L. Lutterotti, E. Manakova, J. Butkus, P. Moeck and A. Le Bail, *J. Appl. Crystallogr.*, 2009, **42**, 726–729.

54 T. Hu and J. Hong, *J. Appl. Phys.*, 2015, **118**, 054301.

55 X. Xiao, M. Wang, J. Tu and S. Jiao, *Phys. Chem. Chem. Phys.*, 2019, **21**, 7021–7028.

56 A. Kokalj, *J. Mol. Graph. Model.*, 1999, **17**, 176–179.

57 P. E. Blöchl, *Phys. Rev. B*, 1994, **50**, 17953.

58 G. Kresse and D. Joubert, *Phys. Rev. B*, 1999, **59**, 1758–1775.

59 A. D. Becke, *J. Chem. Phys.*, 1986, **85**, 7184–7187.

60 J. P. Perdew, K. Burke and M. Ernzerhof, *Phys. Rev. Lett.*, 1996, **77**, 3865–3868.

61 P. Giannozzi, O. Andreussi, T. Brumme, O. Bunau, M. B. Nardelli, M. Calandra, R. Car, C. Cavazzoni, D. Ceresoli and M. Cococcioni, *J. Condens. Matter Phys.*, 2017, **29**, 465901.

62 A. D. Becke and E. R. Johnson, *J. Chem. Phys.*, 2007, **127**, 154108.

63 E. R. Johnson, in *Non-covalent Interactions in Quantum Chemistry and Physics*, ed. A. Otero-de-la-Roza and G. A. DiLabio, Elsevier, 2017, ch. 5, pp. 169–194.

64 A. Otero-de-la-Roza and E. R. Johnson, *J. Chem. Phys.*, 2012, **136**, 174109.

65 A. Otero-de-la-Roza, L. M. LeBlanc and E. R. Johnson, *J. Phys. Chem. Lett.*, 2020, **11**, 2298–2302.

66 E. Koren, I. Leven, E. A. Knoll, O. Hod and U. Duerig, *Nat. Nanotechnol.*, 2016, **11**, 752–757.

67 Z. Yu, A. Song, L. Sun, Y. Li, L. Gao, H. Peng, T. Ma, Z. Liu and J. Luo, *Small*, 2020, **16**, 1902844.